

The Chandra view of the Largest Quasar Lens SDSS J1029+2623

Naomi Ota,¹ Masamune Oguri,² Xinyu Dai,³ Christopher S. Kochanek,⁴ Gordon T. Richards,⁵ Eran O. Ofek,⁶ Roger D. Blandford,⁷ Tim Schrabback,⁸ and Naohisa Inada⁹

Received _____; accepted _____

¹Department of Physics, Nara Women's University, Kitauoyanishimachi, Nara, Nara 630-8506, Japan.

²Kavli Institute for the Physics and Mathematics of the Universe, University of Tokyo, 5-1-5 Kashiwa-no-ha, Kashiwa, Chiba 277-8568, Japan.

³Homer L. Dodge Department of Physics and Astronomy, University of Oklahoma, Norman, OK 73019, USA.

⁴Department of Astronomy, The Ohio State University, Columbus, OH 43210, USA.

⁵Department of Physics, Drexel University, 3141 Chestnut Street, Philadelphia, PA 19104, USA.

⁶Benozio Center for Astrophysics, Weizmann Institute of Science, 76100 Rehovot, Israel.

⁷Kavli Institute for Particle Astrophysics and Cosmology, 2575 Sand Hill Rd., Menlo Park, CA 94309, USA.

⁸Kavli Institute for Particle Astrophysics and Cosmology, Stanford University, 382 Via Pueblo Mall, Stanford, CA 94305-4060, USA

⁹Department of Physics, Nara National College of Technology, Yamatokohriyama, Nara 639-1080, Japan.

ABSTRACT

We present results from *Chandra* observations of the cluster lens SDSS J1029+2623 at $z_l = 0.58$, which is a gravitationally lensed quasar with the largest known image separation. We clearly detect X-ray emission both from the lensing cluster and the three lensed quasar images. The cluster has an X-ray temperature of $kT = 8.1_{-1.2}^{+2.0}$ keV and bolometric luminosity of $L_X = 9.6 \times 10^{44}$ erg s $^{-1}$. Its surface brightness is centered near one of the brightest cluster galaxies, and it is elongated East-West. We identify a subpeak North-West of the main peak, which is suggestive of an ongoing merger. Even so, the X-ray mass inferred from the hydrostatic equilibrium assumption appears to be consistent with the lensing mass from the Einstein radius of the system. We find significant absorption in the soft X-ray spectrum of the faintest quasar image, which can be caused by an intervening material at either the lens or source redshift. The X-ray flux ratios between the quasar images (after correcting for absorption) are in reasonable agreement with those at optical and radio wavelengths, and all the flux ratios are inconsistent with those predicted by simple mass models. This implies that microlensing effect is not significant for this system and dark matter substructure is mainly responsible for the anomalous flux ratios.

Subject headings: galaxies: clusters: general — gravitational lensing: strong — quasars: individual (SDSS J1029+2623) — X-rays: galaxies

1. Introduction

The gravitational lens SDSS J1029+2623 consists of three images of a $z_s = 2.197$ quasar produced by a foreground cluster at $z_l \approx 0.58$ (Inada et al. 2006; Oguri et al. 2008). With a maximum image separation of $22''5$, this is the largest lens among ~ 130 gravitationally lensed quasars known to date. The lensing interpretation is secure from multiple observational facts, including the remarkably similar optical spectra with mini broad absorption line (BAL) features in their emission lines, similar radio loudnesses (Kratzer et al. 2011), and the identification of the lensing cluster in the optical and with weak lensing (Oguri et al. 2012). Furthermore, this lens system represents a rare example of a naked cusp lens. In this configuration, only three images with similar brightnesses are produced on the same side of the lens potential, which is very rare among galaxy-scale quasar lenses (e.g., Lewis et al. 2002) but has been predicted to be fairly common among cluster-scale lenses (Oguri & Keeton 2004; Li et al. 2007; Minor & Kaplinghat 2008).

SDSS J1029+2623 is one of two examples of large-separation quasar lenses produced by massive clusters of galaxies. The other large-separation lens is SDSS J1004+4112 (Inada et al. 2003; Oguri et al. 2004; Sharon et al. 2005; Inada et al. 2005), which consists of five lensed images of a quasar at $z = 1.734$ and a lensing cluster at $z = 0.68$. In fact, these clusters can be regarded as unique examples of *strong-lens-selected* clusters in the sense that they have been identified by searching for strong lenses in a large sample of quasars. In particular, the uniqueness of the selection of these lenses begs the questions of (1) do the strong-lens-selected clusters follow empirical scaling relations derived from optical/X-ray selected clusters? and (2) what is the dynamical state of these clusters?

Chandra and *XMM-Newton* observations of the other large-separation quasar lens, SDSS J1004+4112, have shown that the lensing cluster is relaxed, with the X-ray temperature and luminosity being consistent with the predictions of empirical scaling

relations within the observed scatter (Ota et al. 2006b; Lamer et al. 2006). This interpretation is also supported by the recent comparison of the X-ray measurements with detailed strong lens models (Oguri 2010). There is excellent agreement on the centroids and position angles between the inferred dark matter distribution, the X-ray surface brightness, and the brightest cluster galaxy. On the other hand, the available observational data suggest that the lensing cluster of SDSS J1029+2623 may be complicated. For instance, the existence of two bright elliptical galaxies at the center with a large velocity difference ($\sim 2800 \text{ km s}^{-1}$) between them indicates a possible merger, although it can also be a chance projection of different halos along the line-of-sight. It may be that there is a possible elongation of the mass distribution along line-of-sight, which can be tested by comparing X-ray and lensing-derived masses.

In addition to the properties of the lensing cluster, the high-resolution *Chandra* observations provide an additional probe of the anomalous flux ratios between the quasar images. Oguri et al. (2008) pointed out that observed optical flux ratios of the three quasar images (named image A, B, and C) are markedly different from what simple mass models predict. Kratzer et al. (2011) found that the anomalous flux ratio persists in the radio image for which the effects of differential dust extinction and microlensing by stars are less important. In particular, there is a large flux difference between the close quasar image pair near a fold caustic (images B and C), which implies that a large part of the flux anomaly is caused by (sub-)structure in the mass distribution of the lensing cluster (Kratzer et al. 2011). However, there is a clear wavelength dependence to the optical flux ratios (Oguri et al. 2008), which indicates that chromatic microlensing or dust extinction must also affect the third quasar image especially in optical.

In this paper, we present results from *Chandra* observations of this unique cluster-scale quasar lens. We successfully detected X-ray emission from both the lensing cluster and the

three quasar images, which are discussed in §3 and §4, respectively. We compare our results with observations at other wavelengths, as well as strong lensing information from the quasar images. Throughout the paper we adopt a cosmological model with matter density $\Omega_M = 0.27$, cosmological constant $\Omega_\Lambda = 0.73$, and Hubble constant $H_0 = 70 \text{ km s}^{-1} \text{ Mpc}^{-1}$. At the cluster redshift of $z = 0.584$, $1''$ corresponds to 6.69 kpc. Unless otherwise specified, quoted errors indicate the 90% confidence range.

2. Observations

SDSS J1029+2623 was observed for 60 ks with the *Chandra* Advanced CCD Imaging Spectrometer (ACIS; Garmire et al. 2003) on 2010 March 11 (Observation ID: 11755). The data were obtained with the ACIS S3 CCD operating in VFAINT mode. ACIS-S was chosen because it has higher sensitivity than ACIS-I and that the cluster emission is expected to be *soft* due to the high redshift of the system. This CCD has a 1024×1024 pixel format with an image scale of $0''.492 \text{ pixel}^{-1}$. The target was offset from the nominal aim point with a Y-offset of $-1'$, which has little effect on the spatial resolution. The CCD temperature during the observations was -120°C . The data were processed using the standard software packages CIAO 4.3 and CALDB 4.4.1. The background was stable during the observation and the net exposure time after applying standard light-curve screening cuts was 55815 s.

The ACIS image in the 0.5–7 keV band is shown in Figure 1. The extended cluster emission and the three images of SDSS J1029+2623 are all detected. The astrometry offset is found to be negligibly small ($0''.2$) from the comparison of quasar A position with the optical image. The cluster emission exhibits a somewhat elongated feature, which we will study in detail in §3.2. In the ACIS-S3 field, 42 point-like sources, including the three quasar images, were detected with the `wavdetect` algorithm using a significance threshold

parameter¹ of 10^{-6} .

3. Lensing cluster

3.1. Spectral analysis

We derive the spectrum of the cluster component by extracting the data from a circular region with a radius of $1'$ centered on the X-ray centroid, which is chosen so as to enclose about 90% of source photons and to avoid low signal-to-noise regions in the outskirts. We exclude $5''$ radius regions around each quasar image. The background was estimated in a surrounding annulus ($2.2 < r < 2.5$), rather than using blank-sky observations because the background intensity generally depends on the direction of the sky and time. The 0.5–7 keV source count rate within $r < 1'$ is 0.068 ± 0.001 counts s^{-1} , after the background subtraction. In total, there are ~ 4800 net photons, whereas the background contribution to the total spectrum is about 20%. We fit the cluster spectrum in the 0.5–7 keV band with the APEC thin-thermal plasma model (Smith et al. 2001) utilizing XSPEC version 12.6.0q. The spectral data was rebinned so that each bin contains more than 25 counts and the chi-square statistics was utilized in the fitting. The Galactic hydrogen column density was fixed to $N_{\text{H}} = 1.67 \times 10^{20} \text{cm}^{-2}$ based on the LAB survey (Kalberla et al. 2005). Given the good agreement between the X-ray emission centroid and the position of G2 galaxy (see below), we set the cluster redshift to that of G2 ($z = 0.584$; Oguri et al. 2008). We note that, when the hydrogen column density or the cluster redshift is not fixed but is fitted to the spectrum, the resulting values are consistent with those adopted here.

¹The sigthresh parameter is the significance threshold for source detection and is proportional to the inverse of the number of pixels in the image. A sigthresh parameter of 10^{-6} means that ~ 1 false source per field is allowed.

The cluster spectrum is shown in Figure 2. From the spectral fits the X-ray temperature is constrained to be $kT = 8.1_{-1.2}^{+2.0}$ keV and the metal abundance to be $Z = 0.21Z_{\odot}$ (the 90% upper limit is $0.44Z_{\odot}$). This high temperature indicates that the lensing cluster is indeed massive enough to be capable of producing the large-separation lensed quasar images (see also §3.3). The reduced chi-square of the best-fit model is $\chi^2/\text{dof} = 138/139$, and the parameters of the fit are summarized in Table 1.

The absorption-corrected 0.5–7 keV flux is $4.6 \times 10^{-13} \text{erg s}^{-1}$ ($r < 1'$). The bolometric X-ray luminosity within r_{500} is estimated as $L_X = 9.6 \times 10^{44} \text{erg s}^{-1}$, where r_{500} is defined as the radius within which the average matter density is equal to $\Delta_c = 500$ times the critical density of the Universe at the cluster redshift. The β -model analysis in §3.2 yields $r_{500} = 1.09$ Mpc. This luminosity is lower than the mean value expected from the luminosity-temperature relation of distant clusters, $L_X = 4.0 \times 10^{45} \text{erg s}^{-1}$ (Ota et al. 2006a), but it is within the observed scatter of the $L_X - T$ relation.

To investigate the radial temperature profile, we also analyze spectra for the inner $r < 0'.25$ (~ 100 kpc) region and the outer $0'.25 < r < 1'$ region of the lensing cluster. The fitted temperatures are $kT = 9.8_{-2.1}^{+3.7}$ keV and $6.8_{-1.2}^{+1.7}$ keV, respectively. While the temperature profile is consistent with being constant with radius, the possible decrease of the temperature toward large radii implies that the lensing cluster lacks a cool core that is commonly seen in relaxed clusters (Arnaud et al. 2010), although there is a possibility that a subpeak discussed in §3.2 is in fact a cool core of this cluster.

3.2. Image analysis

The X-ray centroid position (10:29:12.47, +26:23:33.2), measured in §3.2, agrees well with the position of the central galaxy G2 at (10:29:12.48, +26:23:32.0; Inada et al. 2006).

We first fit a single one-dimensional radial surface-brightness profile to the extended X-ray emission. We centered the model at the X-ray centroid and azimuthally averaged the 0.5–5 keV image. We exclude > 5 keV because the significance of X-ray emission above 5 keV is low (see Figure 2). We corrected for vignetting and the detector response using the exposure map calculated for the spectral energy distribution of the cluster. The image was rebinned by a factor of two so that the pixel scale is $0''.98$ (6.58 kpc at the cluster redshift). The quasar images were masked out using a $5''$ radius when calculating the profile.

We fit the radial profile with the following two models: (1) a conventional β -model $S(r) = S_0[1 + (r/r_c)^2]^{-3\beta+1/2}$, and (2) a profile derived from the universal mass profile proposed by Navarro et al. (1997) plus isothermality of the cluster (equations 29–32 in Suto et al. 1998, hereafter NFW-SSM). The background level, which was assumed to be a constant, is simultaneously fit. As illustrated in Figure 3, we find that both models can fit the observed radial profile reasonably well, with reduced chi-square values of $\chi^2/\text{dof} = 183.2/196$ and $178.9/196$ for the β -model and NFW-SSM model, respectively. Note that the extent of the X-ray emission above the 3σ background level is derived as $r_X = 130'' (= 874)$ kpc. The fitted values of the β -model parameters are $\beta = 0.72_{-0.04}^{+0.05}$ and $r_c = 16.4_{-1.6}^{+1.8}$ arcsec ($= 109_{-11}^{+12}$ kpc), while the NFW-SSM model parameters are $B = 12.2_{-1.2}^{+1.6}$ and $r_s = 78_{-11}^{+16}$ arcsec ($= 519_{-77}^{+104}$ kpc). Note B is defined by $B \equiv 4\pi G\mu m_p \rho_s r_s^2 / kT$ and related to the outer slope of the radial profile (Suto et al. 1998).

In the β -model, the central electron density is $n_{e0} = (1.5 \pm 0.1) \times 10^{-2} \text{ cm}^{-3}$. This implies a radiative cooling time at the cluster center of $t_{\text{cool}} = 5.8_{-0.9}^{+1.1}$ Gyr. Here n_{e0} and t_{cool} are derived following basically the same way described in §5.2.1 of Ota & Mitsuda (2004). The cooling time is shorter than the Hubble time but comparable to the age of the Universe at the cluster redshift, $t_{\text{age}} = 8.2$ Gyr. Therefore, radiative cooling should not be important in the cluster core region.

The *Chandra* image suggests that the cluster emission is elongated along the East-West direction. Moreover, there is another emission peak about $10''$ North-West of the cluster centroid (Fig. 1). These motivate us to explore the X-ray surface brightness with two-dimensional models, adopting both the single- and double-component elliptical β -models. The elliptical β -model² is defined by

$$\begin{aligned}
 S(x, y) &= S_0 \left[1 + \left(\frac{r}{r_c} \right)^2 \right]^{-3\beta+1/2} + C, \\
 r(x, y) &= \left[\{(x - x_0) \cos \theta + (y - y_0) \sin \theta\}^2 (1 - \epsilon)^2 \right. \\
 &\quad \left. + \{(y - y_0) \cos \theta - (x - x_0) \sin \theta\}^2 \right]^{1/2} / (1 - \epsilon),
 \end{aligned} \tag{1}$$

where r_c is the core radius, x_0 and y_0 define the cluster center, ϵ is the ellipticity, θ is the position angle, S_0 is the amplitude at the center. The background level per image pixel was fixed to the value obtained from the one-dimensional analysis, $C = 3.3 \times 10^{-9}$ counts s⁻¹ cm⁻².

We first fit a single-component elliptical β -model. The maximum-likelihood fit was performed with *Sherpa*, where the exposure map was included to convolve the model image with the telescope and detector responses. We find that the fit residuals show significant excess emission in the North-West region, as shown in Fig. 4. The parameters and results for the single-component model are summarized in Table 3.

We next consider a two-component model in order to determine the X-ray emission profile of the ICM more precisely. The model consists of two elliptical β -models, one centered on the cluster and the other on the North-West component, plus the constant background. For the North-West component, the parameter β_2 and position angle θ_2 were fixed to 0.7 and 0, respectively, due to the limited photon statistics. The results from fitting the central $3'3 \times 3'3$ region are shown in Table 3 and Figure 5. In order to

²beta2d model in the *Sherpa* fitting package

check the goodness of the fit, we re-binned the image into two single-dimensional profiles in the Right Ascension and Declination directions (Fig. 5, bottom right) and calculated the χ^2 values between the model and data profiles within the central $\pm 1'$ region to find that they are sufficiently small, $\chi^2/\text{dof} = 131/122$ and $148/122$ for the x - and y -directions, respectively. The best-fit cluster-center position of (10:29:12.47, +26:23:33.2) is consistent with G2 (10:29:12.48, +26:23:32.0; Inada et al. 2006) within the errors. The ellipticity of the main cluster component is measured to be $\epsilon = 0.214_{-0.035}^{+0.034}$ (axis ratio $q = 0.786$), which is typical of X-ray surface brightness ellipticities (De Filippis et al. 2005; Flores et al. 2007; Hashimoto et al. 2007; Kawahara 2010; Lau et al. 2012).

Note that there appears to be no optical counterpart for the NW peak at (10:29:11.9, +26:23:37.4). For the APEC model, the X-ray spectrum extracted from $r < 5''$ around the NW peak with subtracted background from the surrounding $5'' < r < 10''$ region yields $kT = 3.8(> 1.7)$ keV and an unabsorbed bolometric luminosity of 1.5×10^{43} erg s $^{-1}$. These parameters are reminiscent of the emission peak detected in the line-of-sight merging system CL0024+17 (Ota et al. 2004). In addition, there is a possible jump in the X-ray surface brightness distribution near the NW peak (Fig. 1). This might be the signature that the NW component is in the process of merging with the main cluster or has recently undergone a merger. These observed features suggest that the NW peak may be a remnant of a merging core or a contact discontinuity so-called cold front (Markevitch et al. 2000; Owers et al. 2009), although the limited photon statistics³ prevent a more detailed exploration.

³The source and background are estimated to be 95 and 163 counts within $r < 5''$, respectively.

3.3. Cluster mass distribution

Under the assumption of hydrostatic equilibrium and spherical symmetry, we can infer the mass distribution of the lensing cluster from the X-ray temperature and surface-brightness profiles. We assume isothermality because we did not detect a significant radial dependence of the X-ray temperature. Figure 6 shows the cylindrical cluster mass projected within a radius r derived from each surface mass distribution profile. We find that both models yield consistent mass profiles within the measurement errors.

For the NFW-SSM model and the critical overdensity $\Delta_c = \Delta_{\text{vir}} = 18\pi^2\Omega^{0.427}$ (Nakamura & Suto 1997), the virial mass and the concentration parameter (defined by the ratio of the virial radius to the scale radius of the NFW profile) are constrained to be $M_{\text{vir}} = 1.57_{-0.39}^{+0.66} \times 10^{15} M_{\odot}$ and $c_{\text{vir}} = 4.52_{-0.58}^{+0.58}$. However, these values should be taken with caution because they rely on the extrapolation of the profiles well beyond the radii where X-ray properties are measured. For comparison with other mass measurements, it may be better to use masses defined for larger critical overdensities Δ_c . In Table 4 we summarize the mass and radius estimated for the virial overdensity and overdensities of $\Delta_c = 500$, 1000, and 2500, for both the β -model and the NFW-SSM model. The result indicates that only r_{2500} is smaller than the extent of the X-ray emission, r_X , presented in §3.2. This means that the results for the other overdensities rely on the extrapolation of the data.

Next we compare the mass distribution derived from the X-ray analysis with those from strong lens models. An issue for strong lens modeling for this cluster has been the uncertainty of the mass centroid, because the naked cusp configuration poorly constrains the center of the mass distribution (Inada et al. 2006; Oguri et al. 2008). Given that the measurement of the X-ray centroid agrees well with the location of one of the brightest cluster galaxies (galaxy G2), it is reasonable to assume that the centroid coincides with galaxy G2, because if the cluster gas is significantly segregated from the dark matter

distribution due to merging (e.g., Markevitch et al. 2004; Bradač et al. 2008) then there should be no correlation between X-ray centroids and bright galaxies that trace the dark matter distribution. We fit the positions of the three quasar images assuming an NFW profile plus external shear model using the software *glafic* (Oguri 2010). We find that the best-fit model predicts the Einstein radius of $\theta_E = 18''.3$ for the source redshift of $z_s = 2.197$. This translates into a cylindrical cluster mass of $M_{2D}(< 122\text{kpc}) = 9.30 \times 10^{13} M_\odot$, which is in good agreement with the enclosed mass derived from the X-ray data (see Figure 6). The rough agreement between lensing and X-ray masses implies that the effect of the line-of-sight elongation of the cluster mass distribution is not significant, despite the fact that possible merging along the line-of-sight suggests a large projection effect. On the other hand, at larger radii ($r \sim 0.5$ Mpc), the X-ray mass is found to be significantly larger than the lensing mass derived from a recent lensing analysis of *Hubble Space Telescope* (HST) data (Oguri et al. in prep.). The mass discrepancy is ascribed to a temperature enhancement due to shock heating during a merger, which might lead to the overestimate of X-ray mass near the Einstein radius. See Oguri et al. in prep. for further discussion.

4. Quasar images

4.1. X-ray properties

Given the small $1''.8$ image separation of images B and C (see Figure 7), we measure the X-ray fluxes and spectra of the quasar images using a circular aperture with a radius of $0''.9$ for all the quasar images. The observed counts in the 0.5–7 keV band are 687, 1073, and 295, for images A–C, respectively. The net contamination from the background and the cluster is estimated to be only a few percent. Similarly the contamination from image B in the extraction radius for image C is estimated to be ~ 10 counts, which is smaller than the 1σ statistical error of the flux of image C. We do not find any clear sign of time variability

for light curves produced with time resolutions of 2048 or 4096 s.

The combined spectrum of the three lensed images A, B, and C is shown in the left panel of Figure 8. We fit the spectrum with a power-law model. The Galactic absorption is again fixed at $N_{\text{H}} = 1.67 \times 10^{20} \text{cm}^{-2}$. We do not find significant intrinsic absorption in the total spectrum. The power-law model is acceptable at the 90% confidence level ($\chi^2/\text{dof} = 57.1/63$) and the power-law index of $\Gamma = 1.55 \pm 0.06$ agrees well with the mean value for mini-BAL quasars observed with *Chandra* (Gibson et al. 2009). The corresponding total luminosity is $5.3 \times 10^{45} \text{ergs s}^{-1}$ in the 2–10 keV band. We do not detect any significant emission from the neutral iron $\text{K}\alpha$ line at 2.0 keV in the observed frame (or 6.4 keV in the rest frame). The 90% upper limit on the equivalent width is $\text{EW} < 170 \text{eV}$ in the quasar rest frame for a power-law combined with a Gaussian line model at 2 keV.

Next we study the spectra of the individual quasar images. We first check the hardness ratios defined by the count rate ratio in the 2–7 keV and 0.5–2 keV bands. The spectral shape of image C differs from A and B because the hardness ratio for image C (0.48 ± 0.06) differs from those of images A (0.37 ± 0.03) and B (0.36 ± 0.02). Indeed, the spectra of images A–C plotted in the right panel of Figure 8 clearly indicate that the emission of image C is heavily absorbed in the soft band. To quantify this, we fit the spectrum with a power-law model absorbed by intervening cold material in addition to the Galactic interstellar medium. Since the location of the cold absorber is not known, we consider cases with the absorber located at either the quasar redshift of $z_s = 2.197$ or at the lens redshift of $z_l = 0.584$.

The result of the power-law plus the absorption model fits are summarized in Table 5. While the inclusion of the additional absorption does not improve the best-fit χ^2 value for images A and B, the fits to image C are significantly improved by including the absorption. We find that the improvement is significant at the $> 99.98\%$ confidence level according to

the F-test ($\Delta\chi^2 = 11$ for one additional parameter), although the redshift of the absorber is not constrained. While the power-law model without the additional absorption for image C appears to be acceptable in the sense that the reduced χ^2 is very close to 1, the resulting power-law slope of $\Gamma = 1.21$ is significantly smaller compared with the best-fit slope of $\Gamma \sim 1.6$ for images A and B. When Γ is fixed to 1.55, which is the best-fit slope for the total quasar spectrum, the reduced χ^2 for image C is $\chi^2/\text{dof}=39.5/26$ without the additional absorption, indicating that the fit is not acceptable at 90% confidence level. We also tried a simultaneous fit to the three spectra with a common intrinsic spectral index Γ , because the intrinsic photon indices are statistically consistent among the three images. The result shown in Table 6 again indicates that the extra absorption is significant only for image C.

4.2. Comparison with optical and radio flux ratios

In Table 7, we compare flux ratios between quasar images measured in the *Chandra* X-ray images with radio and optical flux ratios presented in Kratzer et al. (2011). We find that the absorption corrected flux ratio C/B in the X-ray is larger than the optical flux ratios and is close to the radio flux ratio.

The origin of the absorption may be inferred from the dust-to-gas ratio. Based on the optical spectra of images B and C in Oguri et al. (2008), we estimated a color excess of $E(B - V) \simeq 0.07$ for absorption at $z_s = 2.197$ and $E(B - V) \simeq 0.17$ for absorption at $z_l = 0.584$. These imply dust-to-gas ratios of $E(B - V)/N_H \simeq 2 \times 10^{-24} \text{mag cm}^2 \text{atom}^{-1}$ and $E(B - V)/N_H \simeq 3 \times 10^{-23} \text{mag cm}^2 \text{atom}^{-1}$ at the source and lens redshifts, respectively. The higher value found for dust in the lens is broadly consistent with measurements for other lens systems (Dai & Kochanek 2009), while the value for dust at the source redshift is much lower than expected from this observed correlation. However, such low dust-to-gas ratios appear to be common for intrinsic absorption features of quasars caused by quasar outflow

(Hall et al. 2006), which can be explained by dust evaporation due to irradiation by the central source. Thus we cannot draw any firm conclusion about the origin of the absorption from this analysis. Both the mini-BAL features in the quasar spectrum (see Oguri et al. 2008), which assures the present of outflows in the sightline of this quasar, and the deficiency of dust in the intracluster medium particularly near the center (Chelouche et al. 2007; Muller et al. 2008; Bovy et al. 2008; Kitayama et al. 2009) suggest that intrinsic absorption at the quasar redshift is the more likely scenario, although the anomalous flux ratios imply a faint galaxy near image C which might host the dust at the lens redshift. Indeed, a probable galaxy has recently been identified in the vicinity of image C in the HST image (Oguri et al. in prep.), which might cause the extra absorption detected in image C. If the former interpretation is correct, the different absorptions between image B and C probe spatial variations of the absorption content, possibly related to the structure of disk wind outflows (Green 2006).

We note that the optical C/B flux ratio becomes $C/B \sim 0.4$ once the dust extinction is corrected (see below), which is also consistent with the radio and absorption-corrected X-ray flux ratios. The nearly consistent flux ratios between the radio, optical, and X-ray observations imply that microlensing effect is not significant for this system, particularly because X-ray flux ratios are more easily affected by microlensing (e.g., Ota et al. 2006b; Pooley et al. 2007; Dai et al. 2010).

5. Summary and Discussions

We have presented results from *Chandra* observations of SDSS J1029+2623, the largest-separation gravitational lens system, produced by a cluster of galaxies at $z = 0.58$. We detect significant X-ray emission from the lensing cluster as well as three lensed quasar images.

From the extended cluster emission, the X-ray temperature and bolometric luminosity are constrained to be $kT = 8.1_{-1.2}^{+2.0}$ keV and $L_X = 9.6 \times 10^{44}$ erg s⁻¹. The luminosity is lower than the mean value expected from the luminosity-temperature relation of distant clusters, but it is within the observed scatter of the relation. While the estimated cooling time is shorter than the Hubble time, the lack of a significant temperature drop at the cluster center suggests that radiative cooling is not important in this system. From the image analysis, we have found that the cluster emission is elongated along the East-West direction and has a subpeak in the North-West region. This indicates that the system has undergone a merger. However, the modest ellipticity of the gas distribution found in the main cluster component indicates that the irregularity of mass distribution may not be large. We have reconstructed the mass profile of the lensing cluster, assuming isothermality and hydrostatic equilibrium to find that the X-ray mass within the Einstein radius or ~ 120 kpc is in a good agreement with that expected from the strong lensing. The agreement seems to imply that there is not any significant departure from the equilibrium state in the cluster core, and that the line-of-sight elongation of this cluster may not be so large. On the other hand, the mass discrepancy between the X-ray and lensing measurements was found at larger radii, indicating a complex nature of the mass distribution of this system (Oguri et al. in prep.).

The X-ray spectra of the three quasar images above 2 keV are well represented by a power-law with a photon index of $\Gamma \sim 1.55$ that is typical of mini-BAL quasars. However, significant soft X-ray absorption due to the cold material is detected only in image C. After correcting for the X-ray absorption, the X-ray flux ratios between the quasar images are roughly consistent with those in optical and radio, which suggests that microlensing is not significant for this system. This indicates that the flux ratio anomaly seen in this lens system has to be due to substructure (see, e.g., Kochanek & Dalal 2004). It is difficult to distinguish the possibilities between absorbers at the quasar redshift and at the cluster redshifts from the X-ray spectrum or the dust-to-gas ratio.

Both the surface brightness profile of the lensing cluster and the anomalous flux ratio are better understood by comparing the result with accurate mass modeling results obtained from gravitational lensing analysis. For this purpose we have recently obtained *HST* images of this system. Details of lensing analysis results of the *HST* data and a comparison with the *Chandra* results will be presented in a forthcoming paper (Oguri et al. in prep.).

We thank K. Aoki for useful discussions, and an anonymous referee for many useful suggestions. This work was supported in part by the Grant-in-Aid for Scientific Research by the Ministry of Education, Culture, Sports, Science and Technology, No.22740124 (N.O.). This work was supported in part by the FIRST program “Subaru Measurements of Images and Redshifts (SuMIRe)”, World Premier International Research Center Initiative (WPI Initiative), MEXT, Japan, and Grant-in-Aid for Scientific Research from the JSPS (23740161). C.S.K. is supported by NSF grant AST-1009756. X.D. acknowledges support by NASA/SAO fund GO0-11147B. T.S. acknowledges support from NSF through grant AST-0444059-001 and the Smithsonian Astrophysics Observatory through grant GO0-11147A.

Facilities: CXO (ACIS).

REFERENCES

- Arnaud, M., Pratt, G. W., Piffaretti, R., Böhringer, H., Croston, J. H., & Pointecouteau, E. 2010, *A&A*, 517, A92
- Bovy, J., Hogg, D. W., & Moustakas, J. 2008, *ApJ*, 688, 198
- Bradač, M., Allen, S. W., Treu, T., et al. 2008, *ApJ*, 687, 959
- Chelouche, D., Koester, B. P., & Bowen, D. V. 2007, *ApJ*, 671, L97
- Dai, X., & Kochanek, C. S. 2009, *ApJ*, 692, 677
- Dai, X., Kochanek, C. S., Chartas, G., et al. 2010, *ApJ*, 709, 278
- De Filippis, E., Sereno, M., Bautz, M. W., & Longo, G. 2005, *ApJ*, 625, 108
- Flores, R. A., Allgood, B., Kravtsov, A. V., et al. 2007, *MNRAS*, 377, 883
- Garmire, G.P., Bautz, M.W., Ford, P.G., Nousek, J.A., & Ricker, G.R. 2003, *Proc.SPIE*, 4851, 28
- Gibson, R. R., Brandt, W. N., Gallagher, S. C., & Schneider, D. P. 2009, *ApJ*, 696, 924
- Green, P. J. 2006, *ApJ*, 644, 733
- Hall, P. B., Gallagher, S. C., Richards, G. T., et al. 2006, *AJ*, 132, 1977
- Hashimoto, Y., Böhringer, H., Henry, J. P., Hasinger, G., & Szokoly, G. 2007, *A&A*, 467, 485
- Inada, N., Oguri, M., Pindor, B., et al. 2003, *Nature*, 426, 810
- Inada, N., Oguri, M., Keeton, C. R., et al. 2005, *PASJ*, 57, L7
- Inada, N., et al. 2006, *ApJ*, 653, L97

- Kalberla, P. M. W., Burton, W. B., Hartmann, D., Arnal, E. M., Bajaja, E., Morras, R.,
Pöppel, W. G. L. 2005, *A&A*, 440, 775
- Kawahara, H. 2010, *ApJ*, 719, 1926
- Kitayama, T., et al. 2009, *ApJ*, 695, 1191
- Kochanek, C. S., & Dalal, N. 2004, *ApJ*, 610, 69
- Kratzer, R. M., Richards, G. T., Goldberg, D. M., et al. 2011, *ApJ*, 728, L18
- Lamer, G., Schwobe, A., Wisotzki, L., & Christensen, L. 2006, *A&A*, 454, 493
- Lau, E. T., Nagai, D., Kravtsov, A. V., Vikhlinin, A., & Zentner, A. R. 2012, arXiv:1201.2168
- Lewis, G. F., Carilli, C., Papadopoulos, P., & Ivison, R. J. 2002, *MNRAS*, 330, L15
- Li, G. L., Mao, S., Jing, Y. P., Lin, W. P., & Oguri, M. 2007, *MNRAS*, 378, 469
- Markevitch, M., Ponman, T. J., Nulsen, P. E. J., et al. 2000, *ApJ*, 541, 542
- Markevitch, M., Gonzalez, A. H., Clowe, D., et al. 2004, *ApJ*, 606, 819
- Minor, Q. E., & Kaplinghat, M. 2008, *MNRAS*, 391, 653
- Muller, S., et al. 2008, *ApJ*, 680, 975
- Nakamura, T. T., & Suto, Y. 1997, *Prog. Theor. Phys.*, 97, 49
- Navarro, J. F., Frenk, C. S., & White, S. D. M. 1997, *ApJ*, 490, 493
- Oguri, M. 2010, *PASJ*, 62, 1017
- Oguri, M., & Keeton, C. R. 2004, *ApJ*, 610, 663
- Oguri, M., et al. 2004, *ApJ*, 605, 78

Oguri, M., et al. 2008, *ApJ*, 676, L1

Oguri, M., Bayliss, M. B., Dahle, H., Sharon, K., Gladders, M. D., Natarajan, P., Hennawi, J. F., & Koester, B. P. 2012, *MNRAS*, 420, 3213

Ota, N., Inada, N., Oguri, M., et al. 2006, *ApJ*, 647, 215

Ota, N., Kitayama, T., Masai, K., & Mitsuda, K. 2006, *ApJ*, 640, 673

Ota, N., & Mitsuda, K. 2004, *A&A*, 428, 757

Ota, N., Pointecouteau, E., Hattori, M., & Mitsuda, K. 2004, *ApJ*, 601, 120

Owers, M. S., Nulsen, P. E. J., Couch, W. J., & Markevitch, M. 2009, *ApJ*, 704, 1349

Pooley, D., Blackburne, J. A., Rappaport, S., & Schechter, P. L. 2007, *ApJ*, 661, 19

Sharon, K., Ofek, E. O., Smith, G. P., et al. 2005, *ApJ*, 629, L73

Smith, R. K., Brickhouse, N. S., Liedahl, D. A., & Raymond, J. C. 2001, *ApJ*, 556, L91

Suto, Y., Sasaki, S., & Makino, N. 1998, *ApJ*, 509, 544

Table 1: APEC Models of the Overall Spectrum

Parameter	Value (90% error)
N_{H} (cm^{-2})	1.67×10^{20} (F)
kT (keV)	8.1 (6.8 – 10.1)
Abundance (Z_{\odot})	0.22 (< 0.44)
Redshift	0.584 (F)
Normalization ^a	$7.31 (6.93 - 7.68) \times 10^{-4}$
χ^2/dof	47.5/45
$f_{\text{X},0.5-7}$ ($\text{erg s}^{-1} \text{cm}^{-2}$) ^b	4.6×10^{-13}
$L_{\text{X},0.5-7}$ (erg s^{-1}) ^c	5.5×10^{44}
$L_{\text{X,bol}}$ (erg s^{-1}) ^d	9.6×10^{44}

^aNormalization factor for the APEC model, $\int n_e n_{\text{H}} dV / 4\pi D_A^2 (1+z)^2$ in 10^{-14}cm^{-5} , where D_A is angular size distance to the cluster.

^bGalactic absorption-corrected X-ray flux in the 0.5–7 keV band within $r < 1'$.

^cGalactic absorption-corrected X-ray luminosity in the 0.5–7 keV band within $r < 1'$.

^dBolometric luminosity within r_{500} .

(F) Fixed parameters.

Table 2. Results for Circularly Symmetric Models

Model	Parameter	Value
β -model	S_0 (counts s ⁻¹ cm ⁻² kpc ⁻²) ^a	$3.57_{-0.26}^{+0.28} \times 10^{-9}$
	β	$0.72_{-0.04}^{+0.05}$
	r_c (arcsec/kpc)	$16.4_{-1.6}^{+1.8}/109_{-11}^{+12}$
	χ^2/dof	183.2/196
NFW-SSM model	S_0 (counts s ⁻¹ cm ⁻² kpc ⁻²) ^a	$4.03_{-0.39}^{+0.31} \times 10^{-9}$
	B	$12.2_{-1.2}^{+1.6}$
	r_s (arcsec/kpc)	$78_{-11}^{+16}/519_{-77}^{+104}$
	χ^2/dof	178.9/196

Table 3. Results for Elliptical Models

Model	Parameter	Value
Single elliptical β -model	$x_{0,1}, y_{0,1}$	10:29:12.395, +26:23:33.71 ^a
	S_0 (counts s ⁻¹ cm ⁻² kpc ⁻²)	$3.57_{-0.25}^{+0.28} \times 10^{-9}$
	β	$0.70_{-0.03}^{+0.04}$
	r_c (arcsec/kpc)	$17.6_{-1.6}^{+1.7}/118_{-10}^{+12}$
	ϵ	$0.214_{-0.035}^{+0.034}$
	θ	$0.36_{-0.09}^{+0.09}$
Double elliptical β -model	$x_{0,1}, y_{0,1}$	10:29:12.471, +26:23:33.24 ^b
	$S_{0,1}$ (counts s ⁻¹ cm ⁻² kpc ⁻²)	$3.15_{-0.61}^{+0.36} \times 10^{-9}$
	β_1	$0.71_{-0.04}^{+0.04}$
	$r_{c,1}$ (arcsec/kpc)	$19.0_{-1.9}^{+2.4}/127_{-13}^{+16}$
	ϵ_1	$0.214_{-0.035}^{+0.034}$
	θ_1	$0.36_{-0.09}^{+0.09}$
	$x_{0,2}, y_{0,2}$	10:29:11.853, +26:23:37.37 ^c
	$S_{0,2}$ (counts s ⁻¹ cm ⁻² kpc ⁻²)	$3.1_{-1.2}^{+2.3} \times 10^{-9}$
	β_2	0.70(F)
	$r_{c,2}$ (arcsec/kpc)	$3.9_{-1.7}^{+4.1}/26_{-12}^{+28}$
	ϵ_2	0.19(< 0.35)
	θ_2	0.0(F)

^aThe 90% errors are $\pm 1''.1$ for x_0 and $\pm 1''.0$ for y_0 .

^bThe 90% errors are $\pm 1''.4$ for $x_{0,1}$ and $\pm 1''.1$ for $y_{0,1}$.

^cThe 90% errors are $\pm 1''.7$ for $x_{0,2}$ and $\pm 1''.5$ for $y_{0,2}$.

Table 4: Masses for Different Critical Overdensities

Model	$M_{\text{vir}}^{\text{a}}$	$r_{\text{vir}}^{\text{b}}$	M_{500}^{a}	r_{500}^{b}	M_{1000}^{a}	r_{1000}^{b}	M_{2500}^{a}	r_{2500}^{b}
β	$12.95_{-3.07}^{+5.00}$	$2.10_{-0.18}^{+0.24}$	$6.68_{-1.59}^{+2.60}$	$1.09_{-0.09}^{+0.13}$	$4.65_{-1.11}^{+1.83}$	$0.77_{-0.07}^{+0.09}$	$2.81_{-0.68}^{+1.13}$	$0.48_{-0.04}^{+0.06}$
NFW-SSM	$15.67_{-3.93}^{+6.55}$	$2.24_{-0.21}^{+0.28}$	$9.28_{-2.41}^{+3.93}$	$1.22_{-0.12}^{+0.15}$	$6.45_{-1.72}^{+2.81}$	$0.86_{-0.08}^{+0.11}$	$3.52_{-0.99}^{+1.62}$	$0.52_{-0.05}^{+0.07}$

^aIn units of $10^{14}M_{\odot}$.

^bIn units of Mpc.

Table 5: Absorbed Power-law Models for the Quasar Images

Name	No extra absorption		Absorption at $z = 2.197$			Absorption at $z = 0.584$		
	Γ	χ^2/dof	Γ	N_{H}^{a}	χ^2/dof	Γ	N_{H}^{a}	χ^2/dof
A	$1.56^{+0.12}_{-0.11}$	31.3/33	$1.56^{+0.16}_{-0.11}$	0.00(< 0.70)	31.3/32	$1.56^{+0.16}_{-0.11}$	0.00(< 0.12)	31.3/32
B	$1.68^{+0.09}_{-0.09}$	23.2/33	$1.68^{+0.10}_{-0.09}$	0.00(< 0.33)	23.2/32	$1.68^{+0.10}_{-0.09}$	0.00(< 0.06)	23.2/32
C	$1.21^{+0.14}_{-0.14}$	25.1/25	$1.68^{+0.32}_{-0.28}$	$3.13^{+2.24}_{-1.68}$	13.5/24	$1.71^{+0.34}_{-0.30}$	$0.54^{+0.40}_{-0.30}$	14.1/24
Total	$1.55^{+0.06}_{-0.06}$	57.1/63	$1.55^{+0.10}_{-0.06}$	0.00(< 0.46)	57.1/62	$1.55^{+0.10}_{-0.06}$	0.00(< 0.08)	57.1/62

^aThe hydrogen column density in the unit of $[10^{22} \text{ cm}^{-2}]$.

Table 6: Joint fits to the Quasar Spectra

Name	Absorption at $z = 2.197$			Absorption at $z = 0.584$		
	Γ	N_{H}^{a}	χ^2/dof	Γ	N_{H}^{a}	χ^2/dof
A	$1.65^{+0.08}_{-0.08}$	0.24(< 0.89)	69.4/90	$1.65^{+0.08}_{-0.08}$	0.04(< 0.15)	70.0/90
B		0.00(< 0.25)			0.00(< 0.04)	
C		$2.97^{+1.38}_{-1.08}$			$0.49^{+0.22}_{-0.18}$	

^aThe hydrogen column density in the unit of $[10^{22} \text{ cm}^{-2}]$.

Table 7. X-ray and optical properties of SDSS J1029+2623

Name	$F_X^{a,b}$	hardness ^c	α_{ox}	$f(\text{X})^{b,d}$	$f(\text{opt}, V)^d$	$f(\text{opt}, I)^d$	$f(\text{radio})^d$
A	0.90 ± 0.03 (0.89)	0.37 ± 0.03	-1.32	0.66 (0.64)	0.96	0.95	0.80 ± 0.06
B	1.37 ± 0.04 (1.34)	0.36 ± 0.02	-1.26	$\equiv 1$	$\equiv 1$	$\equiv 1$	$\equiv 1$
C	0.49 ± 0.03 (0.40)	0.48 ± 0.06	-1.14	0.36 (0.27)	0.16 ^e	0.24 ^e	0.46 ± 0.05

^aAbsorption-corrected, 0.5–7 keV X-ray flux in units of $10^{-13} \text{erg s}^{-1} \text{cm}^{-2}$ and the 1- σ error.

^bThe value in the parenthesis are those without absorption corrections.

^cHardness ratios defined by the count rate ratios in 2 – 7 keV and 0.5 – 2 keV bands. Errors indicate 68% confidence limits.

^dFlux normalized by the flux of image B. The optical and radio flux ratios are taken from Kratzer et al. (2011). Statistical errors on the optical flux ratios are $\lesssim 2\%$ (Oguri et al. 2008).

^eThe optical C/B flux ratio becomes $C/B \sim 0.4$ once the dust extinction is corrected.

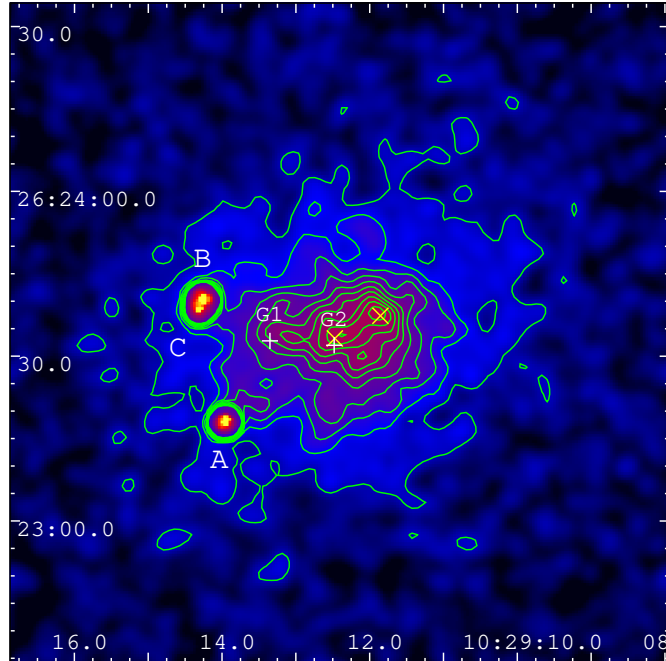


Fig. 1.— Adaptively-smoothed ACIS-S3 image of SDSS J1029+2623 in the 0.5–7 keV band. Both the image and contours are X-ray data. The A–C quasar images of SDSS J1029+2623 and the extended emission from the lensing cluster are seen. The X-ray centroid of the cluster component and the North-West subpeak are marked with an “×” while the positions of the two most luminous galaxies, G1 and G2, are marked with a “+”. The close B/C image pair is resolved in the raw, unsmoothed image (see §4).

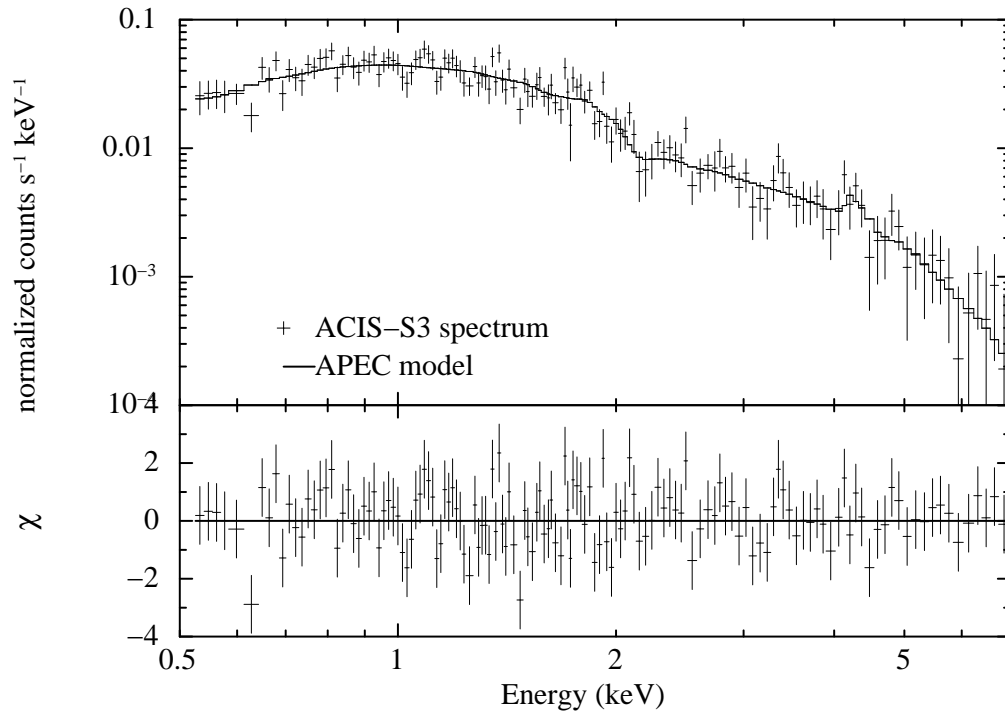


Fig. 2.— *Chandra* ACIS-S3 spectrum of SDSS J1029+2623 ($r < 1'$) fitted with the APEC model. In the top panel, the crosses denote the spectrum in the observed frame and the histogram function shows the best-fit model convolved with the telescope and detector response functions. The bottom panel shows the residuals of the fit in units of σ .

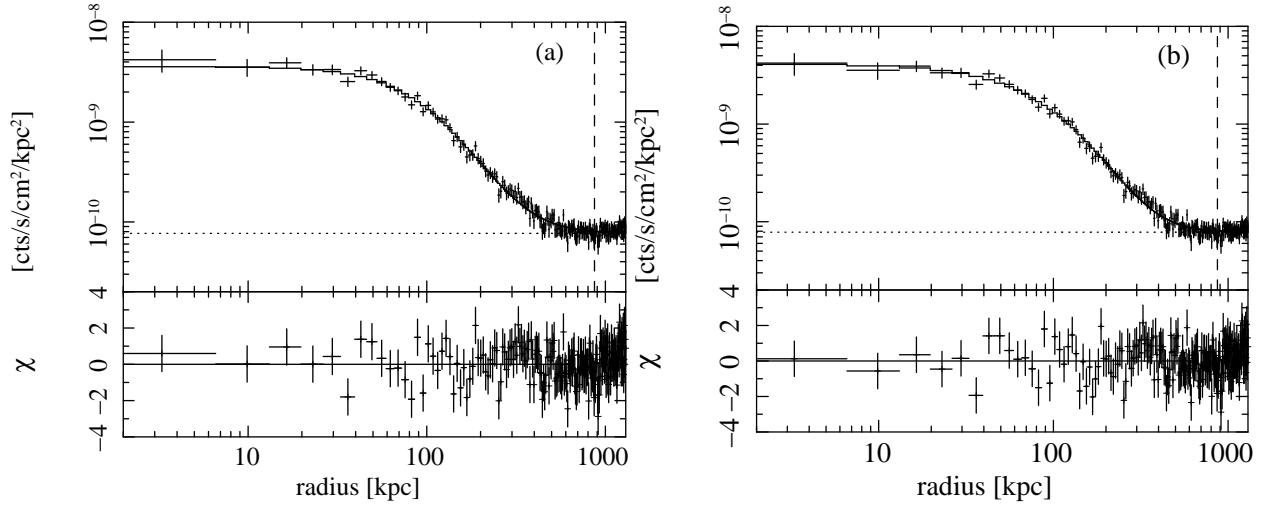


Fig. 3.— Results of the X-ray surface brightness profile fits with (a) the β -model and (b) the NFW-SSM model. In each panel, the crosses show the observed surface brightness in the 0.5–5 keV band and the solid line shows the best-fit model. The background is shown with the horizontal dotted line. The vertical dashed line shows the observed extent of the diffuse X-ray emission, r_X (see text). The bottom panel shows the residuals in units of the local noise.

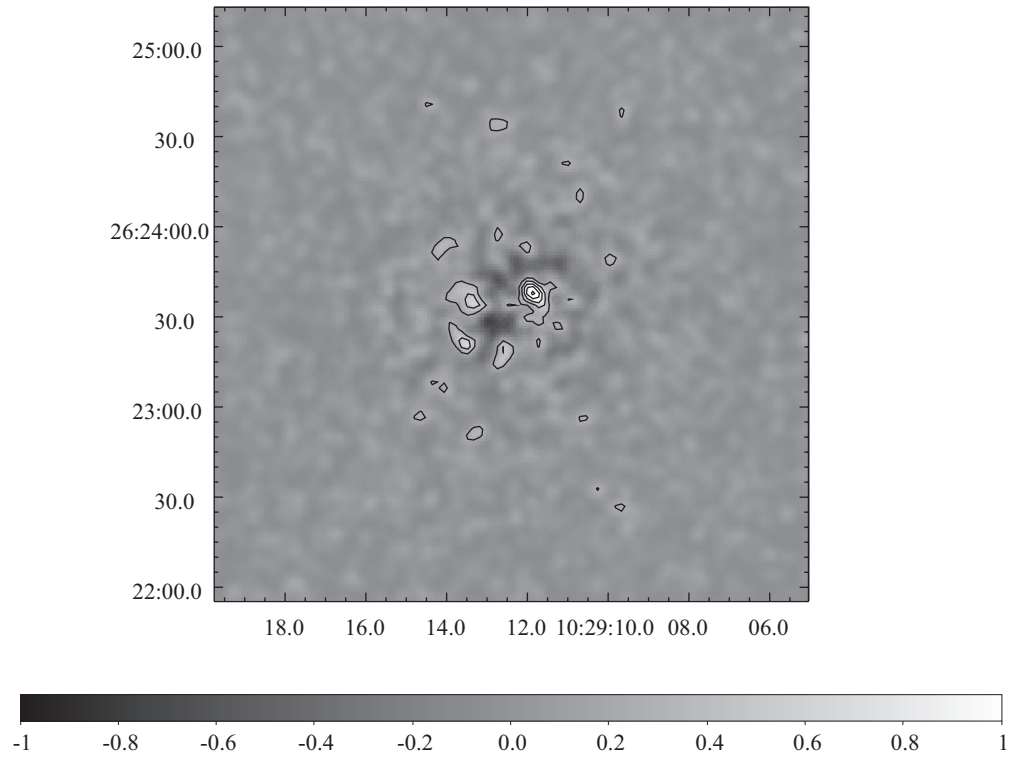


Fig. 4.— Residuals from fits with a single elliptical β -model. The image is smoothed with a $\sigma = 2''$ Gaussian, and excess emission over the best-fit model is shown by the black contours with linear spacing.

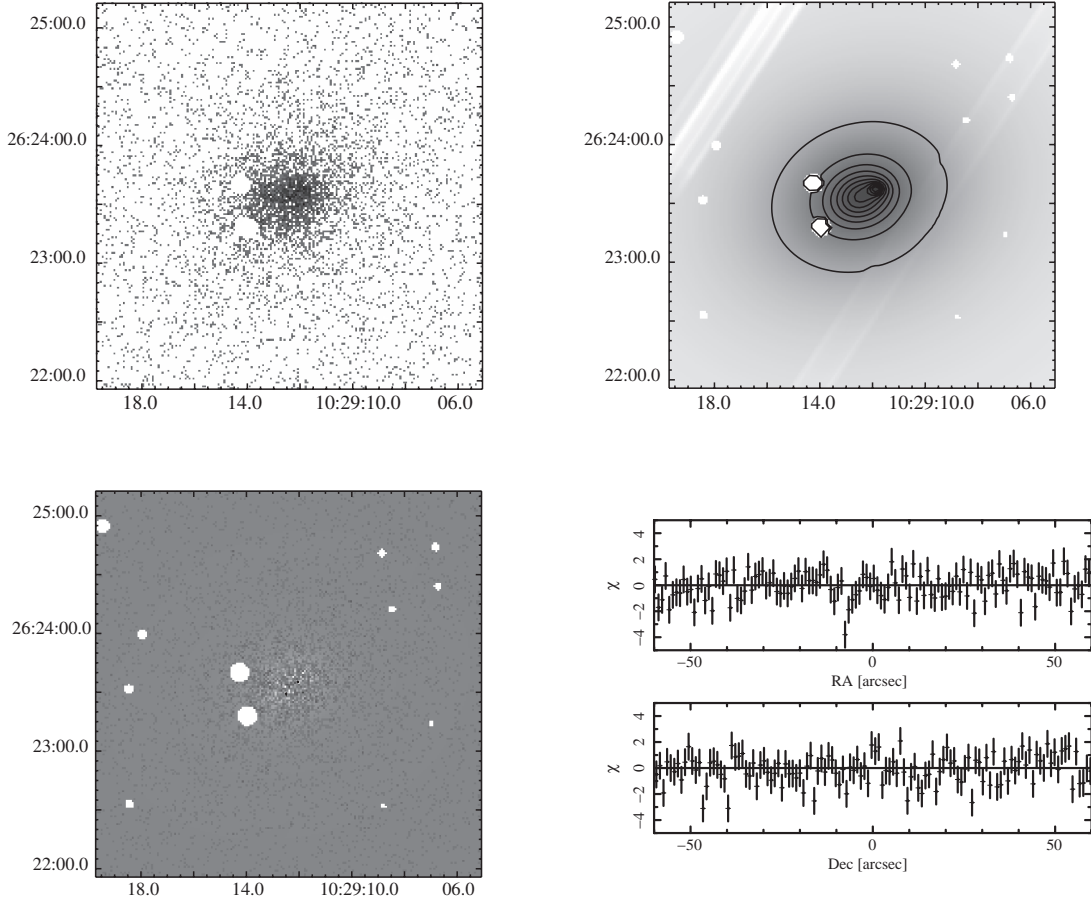


Fig. 5.— Results for the fits with the double elliptical β -model. Top left: *Chandra* ACIS-S3 image of the central $3'.3 \times 3'.3$ region of SDSS J1029+2623 in the 0.5–5 keV energy range. Top right: The best-fitting elliptical β -model, overlaid with logarithmically spaced intensity contours. Bottom left: Residuals from the fit. Bottom right: Residuals along East-West (*top*) and North-South (*bottom*) lines through the cluster center in units of significance.

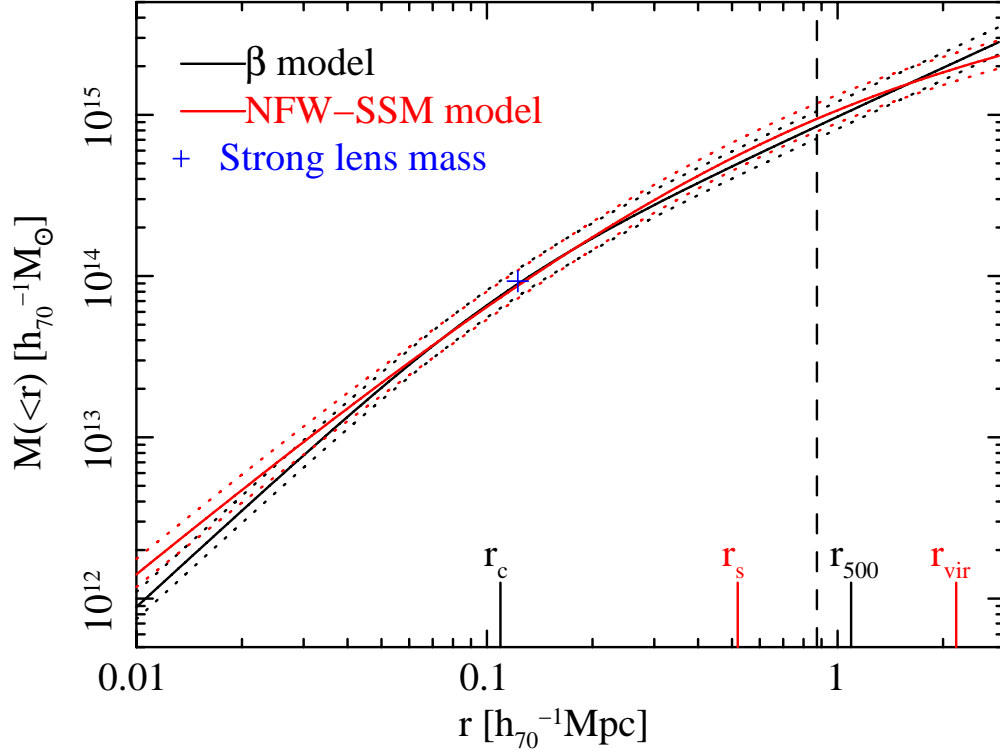


Fig. 6.— Enclosed mass of the lensing cluster, M_X , for the β -model (black) and the NFW-SSM model (red). The dotted lines indicate the 90% error ranges. Note that M_X is a cylindrical cluster mass projected within a radius r . The mass derived from gravitational lensing is also shown for comparison. The meaning of the vertical dashed line is the same as Figure 3.

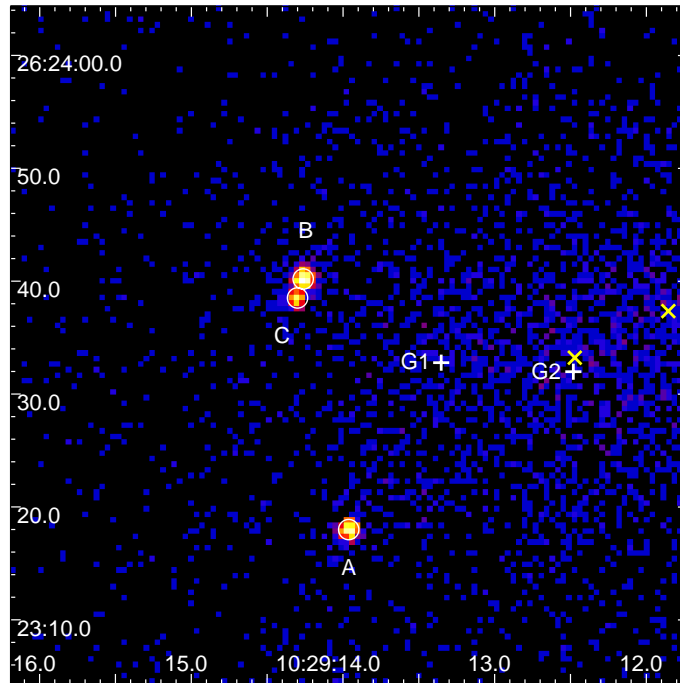


Fig. 7.— Raw ACIS-S3 image of SDSS J1029+2623 in the 0.5–7 keV band. The spectral regions for quasar images A–C are indicated with the circles. The meaning of the labels are the same as Figure 1.

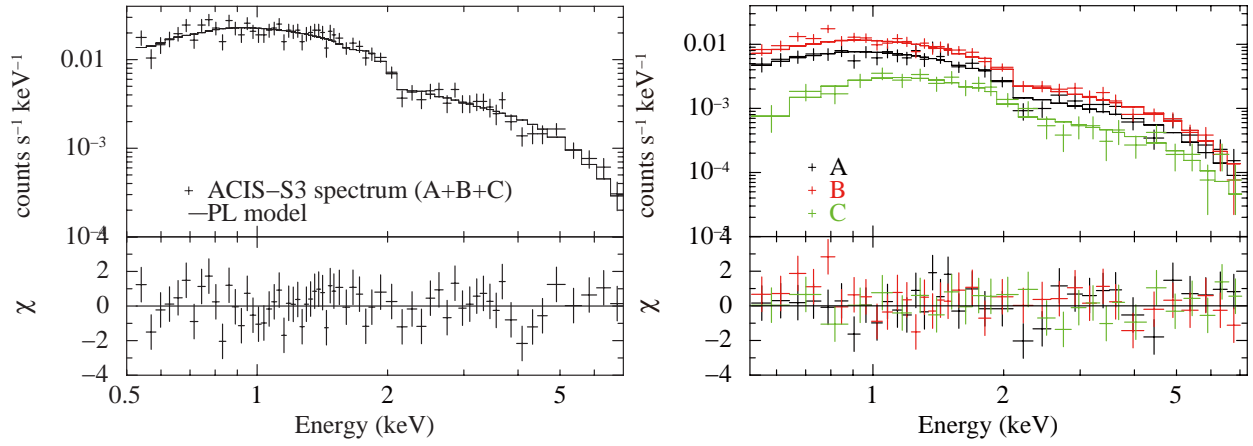


Fig. 8.— Left: total quasar spectrum fit with the power-law model (solid line). Right: Spectra of lensed quasar images A (black), B (red), and C (green) fit with a common intrinsic slope Γ . In each top panel, the crosses denote the spectrum in the observed frame.